J. Fluid Mech. (2002), *vol.* 451, *pp.* 169–191.
DOI: 10.1017/S0022112001006474 Printed in the United Kingdom

Fluidization of 1204 spheres: simulation and experiment

By T.-W. PAN[1], D. D. JOSEPH[2], R. BAI[2], R. GLOWINSKI[1] AND V. SARIN[3]

[1]Department of Mathematics, University of Houston, Houston, TX 77204, USA

[2]Department of Aerospace Engineering and Mechanics, University of Minnesota, Minneapolis, MN 55454, USA

[3]Department of Computer Sciences, Texas A&M University, College Station, TX 77843, USA

(Received 10 April 2000 and in revised form 27 June 2001)

In this paper we study the fluidization of 1204 spheres at Reynolds numbers in the thousands using the method of distributed Lagrange multipliers. The results of the simulation are compared with an experiment. This is the first direct numerical simulation of a fluidized bed at the finite Reynolds numbers encountered in applications. The simulations are processed to give straight lines in log–log plots leading to power laws as in the celebrated experimental correlations of Richardson & Zaki (1954). The numerical method allows the first direct calculation of the slip velocity and other averaged values used in two-fluid continuum models. The computation and the experiment show that a single particle may be in balance with respect to weight and drag for an interval of fluidizing velocities; the expectation that the fluidizing velocity is unique is not realized. The numerical method reveals that the dynamic pressure decreases slowly with the fluidizing velocity. Tentative interpretations of these new results are discussed.

1. Introduction

The current popularity of computational fluid dynamics is rooted in the perception that information implicit in the equations of motion can be extracted without approximation using direct numerical simulation (DNS).

Direct numerical simulation of solid–liquid flows is a way of solving the initial value problem for the motion of particles in fluids. The particles are moved by Newton's laws under the action of hydrodynamic forces computed from the numerical solution of the fluid equations. To perform a direct simulation in the above sense, therefore, one must simultaneously integrate the Navier–Stokes equations (governing the motion of the fluid) and the equations of rigid-body motion (governing the motion of the particles). These equations are coupled through the no-slip condition on the particle boundaries, and through the hydrodynamic forces and torques that appear in the equations of rigid-body motion. These hydrodynamic forces and torques must of course be those arising from the computed motion of the fluid, and so are not known in advance, but only as the integration proceeds. It is crucial that no approximation of these forces and torques be made – other than that due to the numerical discretization itself – so that the overall simulation will yield a solution of the coupled initial value problem upto the numerical truncation error.

Many excellent numerical studies of particulate flows of many particles, which are not direct simulations in the above sense, have appeared in recent years. These approximate methods include simulations based on potential flow, Stokes flow, and point-particle approximations; they all simplify the computation by ignoring some possibly important effects like viscosity and wakes in the case of potential flow, inertial forces which produce lateral migration and across-stream orientations in the case of Stokes flow and the effects of stagnation and separation points in the case of point-particle approximations. Point-particle approximations do advect particles by Newton's law but in some cases the influence of particles on the flow is neglected, in some cases the force on the fluid from the particles is added to the Navier–Stokes equations. Although this approach is often referred to as 'direct simulations' by its practitioners, the forces on each particle are related to its motion and the fluid velocity by semi-empirical relations and this method is only applicable to dilute flows where there are no direct particle–particle interactions.

One goal pursued here is to demonstrate that data from numerical experiments on fluidization can be processed on log–log plots, giving straight lines leading to power laws as did Richardson & Zaki (1954) for real experiments. As far as we know, we are the only group of researchers to carry out this program. There is no prior literature in which power laws are obtained from numerical experiments, On the other hand, there are a number of numerical packages for particles in fluids that might be used in this way. The methods of Stokesian dynamics (see Brady 1993) can be recommended for problems in which inertia is absent. Following earlier work by Wachmann *et al.* (1998) and Wachmann & Schwarzer (1998), Hofler *et al.* (1999) introduced two approximate Euler–Lagrangian simulation methods for particles in fluids. In one method, the particle surface is discretized in grid topology; spheres are polygons on flat plates between nodes. In the second method, a volume force term is introduced to emulate rigid body motion on the particle surface; this method is similar to the force coupling methods introduced by Maxey & Patel (1997). Hofler *et al.* (1999) calculated the sedimentation of 65 000 spheres but at Reynolds numbers so small that it is essentially Stokes flow. Johnson & Tezduyar (1999) used a fully resolved DNS/ALE method to compute the sedimentation of 1000 spheres at Reynolds numbers not larger than 10. A fully resolved method which is based on matching explicit Stokes flow representations of flow near particles with computations on a grid has been proposed by Ory, Oguz & Prosperetti (2000). The problem of particulates in turbulent flows has been considered by a few authors, e.g. Crowe, Chung & Troutt (1996), McLaughlin (1994), and Maxey *et al.* (1997); these approaches use point-particle approximations because fully resolved computations in turbulent flow are not at present possible. Numerical approaches to particulate flow based on the discrete lattice Boltzmann equation have been presented by Ladd (1994*a*, *b*, 1996, 1997), Aidun (1996), Aidun, Lu & Ding (1998) and Qi (1997, 1999).

The correlations of Richardson & Zaki (1954) are an empirical foundation for fluidized bed practice. They performed many experiments with different liquids, gases and particles. They plotted their data on log–log plots; these data fell on straight lines whose slope and intercept could be determined. This showed that the variables follow power laws. This method can also be used for numerical experiments on fluidization and on the lifting of particles across streamlines in Poiseuille flow (see Patankar *et al.* 2001*a*, *b*). The existence of power laws can be regarded as a consequence of similarity (Barenblatt 1996); it is not an obvious consequence of the physics of flow of particulates or of the equations of motion. The possibility that power laws underlie the flows of dispersions generally could be considered.

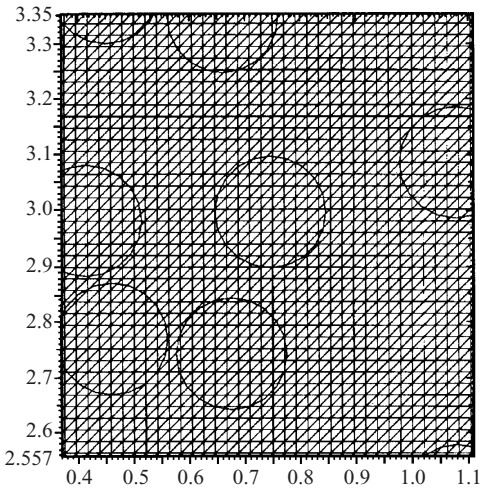

FIGURE 1. Part of a two-dimensional example of a fixed triangular grid used in DLM computation. The same grid covers the fluid and solid. The fluid in the circle is constrained by Lagrange multipliers to move as a rigid body.

In this article, we present the results of a simulation of the fluidization of 1204 spheres which are in satisfying agreement with results obtained by experiments. We will discuss the numerical method briefly in § 2 and then experiments in § 3. In § 4 we present numerical results and compare them with experimental ones in § 5. Section 6 deals with the problem of computing time averages from computations. Section 7 examines the decomposition of the pressure gradient and specifies the variation with solids fraction of the part of the pressure gradient due to wall friction. The Richardson–Zaki correlation from DNS is discussed in §§ 8 and 9.

2. Numerical method

To perform the direct numerical simulation of particulate flow, Glowinski *et al.* (1997, 1998, 1999, 2001) have developed a methodology that is a combination of a distributed Lagrange-multiplier-based fictitious domain method (DLM) and operator splitting methods. The basic idea is to imagine that fluid fills the space inside as well as outside the particle boundaries. The fluid-flow problem is then posed on a larger domain (the 'fictitious domain'). This larger domain is simpler, allowing a simple regular mesh to be used. This in turn allows specialized fast solution techniques. The larger domain is also time-independent, so the same mesh can be used for the entire simulation, eliminating the need for repeated remeshing and projection (see figure 1). This is a great advantage, since for three-dimensional particulate flow the automatic generation of unstructured body-fitted meshes in the region outside a large number of closely spaced particles is a difficult problem. In addition, the entire computation is performed matrix-free, resulting in significant savings.

The velocity on each particle boundary must be constrained to match the rigid-body motion of the particle. In fact, in order to obtain a combined weak formulation with the hydrodynamic forces and torques eliminated, the velocity inside the particle boundary must also be a rigid-body motion. This constraint is enforced using a distributed Lagrange multiplier, which represents the additional body force per unit volume needed to maintain the rigid-body motion inside the particle boundary, much

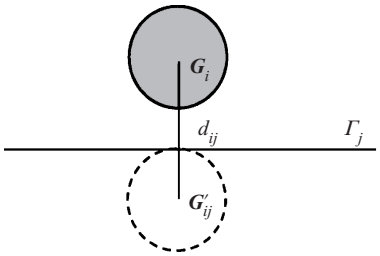

FIGURE 2. Imaginary particle.

like the pressure in incompressible fluid flow whose gradient is the force required to maintain the constraint of incompressibility.

For the space approximation of the problem by finite element methods, we use P_1-*iso*-P_2 and P_1 finite elements for the velocity field and pressure respectively, like Bristeau, Glowinski & Periaux (1987). Then we apply the Marchuk–Yanenko operator-splitting technique discussed in Marchuk (1990) for discretization in time (Operating-splitting schemes have been used for solving the Navier–Stokes equations by many authors, starting, to our knowledge, with Chorin 1967, 1968, 1973.) The linearly constrainted quadratic minimization problems which arise from this splitting are solved using conjugate gradient algorithms, yielding a method that is robust, stable, and easy to implement. For further details, see Glowinski *et al.* (1999). The *immerse boundary methods* of C. Peskin and his collaborators, Peskin (1977, 1981), Peskin & McQueen (1980), for the simulation of incompressible viscous flow in regions with elastic moving boundaries also use a fictitious domain method, but without Lagrange-multipliers.

The statement that DNS fully resolves the solid–liquid flow should be qualified to say that it is resolved up to the treatment of collisions. To prevent particles from penetrating each other or the walls, we adopt the following collision strategy. If we consider the particular case of circular particles in two dimensions or spherical particles in three dimensions, and if B_i and B_j are such two particles, with radii R_i and R_j and centres of mass $\boldsymbol{G}_i$ and $\boldsymbol{G}_j$, we shall require the repulsive force $\boldsymbol{F}_{ij}^p$-between B_i and B_j to satisfy the following properties:

$$\boldsymbol{F}_{ij}^p = \begin{cases} \boldsymbol{0} & \text{if} \quad d_{ij} > R_i + R_j + \rho \\ \dfrac{1}{\varepsilon_p}\left(\dfrac{R_i + R_j + \rho - d_{ij}}{\rho}\right)^2 \dfrac{\boldsymbol{G}_i\boldsymbol{G}_j}{d_{ij}} & \text{if} \quad d_{ij} \leqslant R_i + R_j + \rho, \end{cases} \tag{2.1}$$

where $d_{ij} = |\boldsymbol{G}_i\boldsymbol{G}_j|$, ρ is the force range, and ε_p is a given small positive 'stiffness' parameter chosen so that particles never touch. To treat particle–wall interactions we use a similar approach by introducing an imaginary particle as shown in figure 2, where $d_{ij} = |\boldsymbol{G}_i\boldsymbol{G}'_{ij}|$. The choice of ε_p is discussed in Glowinski *et al.* (2001, § 5). Indeed, the above repulsion force is not part of the problem's description. It is invoked to keep the particles apart. Smooth particles should not collide, as there is always a liquid film; if we do not provide for film rupture, the repulsive lubrication forces become larger and larger as the film becomes smaller.

Fortunately the artificial repulsive force does not seem to have much effect on the global motion (see figure 5). However, the implementation of a security zone has the unfortunate consequence that particles cannot close pack. Though this does not seem to affect fluidized flows greatly, we must be able to generate close packing if we are

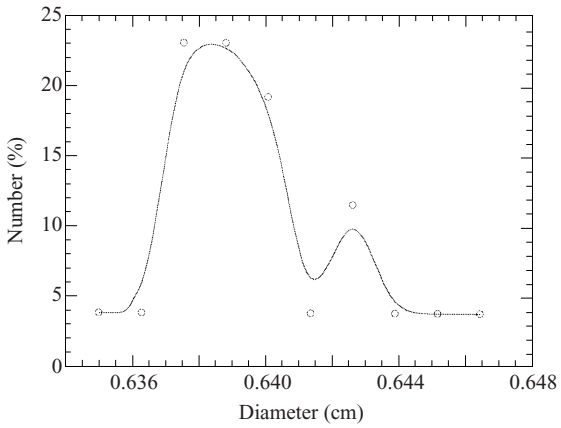

FIGURE 3. Distribution of diameters of spheres used in the fluidization experiment; average = 0.639826 cm.

able to accurately model the frictional resistances between close-packed solids and walls.

We have developed, but not yet implemented, several methods in which repulsive forces are activated only when particles touch; this strategy will allow true tolerance of the mesh.

The DLM approach uses uniform grids for two- and three-dimensional domains, and relies on matrix-free operations on the velocity and pressure unknowns in the domain. This simplifies the distribution of data on parallel architectures and ensures excellent load balance (see Pan *et al.* 1999). The basic computational kernels, vector operations such as additions and dot products and matrix-free matrix-vector-products, yield excellent scalability on distributed shared memory computers such as the SGI Origin 2000. A multilevel parallel elliptic solver (Sarin & Sameh 1998) has been incorporated into the DLM algorithm for two-dimensional fluidized bed problems. This has yielded speed-up of about 6 on 16 processors compared with the elapsed time on two processors on an SGI Origin 2000 at the NCSA. In addition, this represents an impressive eight-fold increase in speed over the best serial implementation. Even though there is a serial component of the three-dimensional code, we have still observed a speed-up of 1.6 on four processors compared with the time on two processors on an SGI Origin 2000. But no further speed-up can be gained if we increase the number of processors from four to eight. All numerical results reported in this article are obtained on four processors on an SGI Origin 2000 at the Minnesota Supercomputing Institute.

3. Experiments

We have carried out experiments on fluidization of 1204 nylon spheres in a slit bed of dimensions

$$[\text{depth, width, height}] = [0.686\,\text{cm}, 20.30\,\text{cm}, 70.22\,\text{cm}].$$

The cross-sectional area of the bed is

$$A = 0.686 \times 20.30 = 13.32\,\text{cm}^2.$$

We could not measure variations of the gap, size inside the bed, but the glass plates were held under pressure against 0.686 cm spacers by aluminium screw clamps. The nominal diameter of the spheres was

$$d = 0.635\,\text{cm}\ (1/4\,\text{in.}).$$

The sphere diameters varied from 0.635 to 0.6465 cm (see figure 3), the average was

$$\bar{d} = 0.639826\,\text{cm}.$$

The density of the spheres is

$$\rho_s = 1.14\,\text{g cm}^{-3}.$$

The spheres were fluidized in water (we did not monitor the room temperature) of density and viscosity

$$\rho_f = 1\,\text{g cm}^{-3}, \quad \eta_f = 0.01\,\text{P}.$$

The Reynolds number based on the fluidization velocity for a single sphere is

$$R = \frac{V(0)d}{\eta_f/\rho_f} \approx 730. \tag{3.1}$$

Local Reynolds numbers in a fluidized suspension can be larger because of the backflow through constriction formed by nearby spheres. A velocity

$$V_2 = 3.00\,\text{cm s}^{-1} \tag{3.2}$$

for incipient fluidization was identified roughly to within $0.1\,\text{cm s}^{-1}$ as the value at which spheres more loosely packed in the fixed bed lifted slightly away from nearby spheres. According to the Richardson–Zaki formula (9.3), the velocity should vary between V_i and $V(0)$:

$$3 = V_i \leqslant V(\phi)V(0) = 11.5\,\text{cm s}^{-1} \tag{3.3}$$

Our experiments were consistent with this inequality.

The water is injected at the bottom of the bed through an array of plastic tubes under a distributor and an eddy dampening screen. The resulting fluidizing velocity is not uniform but there is no evidence of systematic anisotropy as the flow passes through the distributor screen. Large eddies of hydrodynamic origin exactly like the one shown in the 1204 sphere animation at http://www.aem.umn.edu/Solid-Liquid_Flows/ are always present in the experiments. The fluidizing velocity is computed from values of the mass flow rate measured by collecting the weight of the overflow in a beaker over a fixed period of time. The mass flow rate is

$$\rho_f \dot{Q} = W/\Delta t \tag{3.4}$$

where $\dot{Q}$ is the volume flow rate; W is the weight of fluid in the beaker collected over time Δt. The fluidizing (superficial) velocity is

$$V(\phi) = \dot{Q}/A, \tag{3.5}$$

where A is the cross-sectional area of $13.32\,\text{cm}^2$.

The height of the bed is measured by averaging the height of the top layer of particles. Stable bed heights with large fluctuations were typical. The measured values of the bed height as a function of the fluidization velocity $V(\phi)$ are presented in figures 17 and 18 where they are compared with numerical simulation.

The solids fraction at a fluidization velocity $V(\phi)$ is given by inverting the height

$H(\phi)$:

$$\phi = \frac{\Omega_s}{\Omega} = \frac{1204\pi d^3/6}{AH} = \frac{4.437}{H}. \tag{3.6}$$

4. Numerical simulation

The calculation was carried using the distributed Lagrange multiplier method (DLM) described in § 2. The mesh size for velocity is

$$h_V = 0.06858\,\text{cm}$$

so the number of nodes is 3 348 675 ($11 \times 297 \times 1025$). The mesh size for the pressure is $h_p = 2h_V$ (458 622) nodes. The time steps used in the computation are either 0.001 or 0.0005 s, with smaller time steps taken at times when the bed is fully expanded. The main parts of the computation were carried out with a partially parallel code; the computation time for running it is 115 s per time step on four R12000 processors in a SGI Origin 2000 at the Minnesota Supercomputing Institute. For example, the case $V = 4.5\,\text{cm s}^{-1}$ took about 1660 h to reach time $\tau = 26$ s in the simulation; this is 63.84 h of computation time for 1 s of real time.

In the simulation, the initial configuration of particles for the case of $V = 3\,\text{cm s}^{-1}$ is a square lattice; the initial flow field is zero everywhere. Then we used the results of $V = 3\,\text{cm s}^{-1}$ at $t = 13$ (resp., $t = 19.5$) as the initial conditions for the case of $V = 3.5\,\text{cm s}^{-1}$ (resp., $V = 2\,\text{cm s}^{-1}$). For the case of $V = 4\,\text{cm s}^{-1}$ (resp., $V = 4.5\,\text{cm s}^{-1}$), the initial conditions are obtained from the case of $V = 3.5\,\text{cm s}^{-1}$ (resp., $V = 4\,\text{cm s}^{-1}$) at $t = 16.15$ (resp., $t = 2$). And finally for the case $V = 5\,\text{cm s}^{-1}$, the initial conditions are obtained from the case of $V = 4.5\,\text{cm s}^{-1}$ at $t = 27.2$. The above choices of initial conditions explains why the starting values of the bed height for different V are different in figure 4. For the parameters in (2.1) and (2.2), we took

$$\varepsilon_p = 5 \times 10^{-7}, \quad \varepsilon_w = \varepsilon_p, \quad \rho = h_v = 0.06858\,\text{cm}. \tag{4.1}$$

The force range 0.06858 cm is larger than the distance (0.686–0.635)/2 = 0.0255 cm between a centred ball and a sidewall. Hence, in the simulation the balls are effectively centred between the close walls by the particle–wall repulsive force. This centring mechanism is artificial; in the experiments the balls can go closer to one wall or other. Therefore, the drag on the balls in the experiment is larger than the drag in the simulation.

Figure 4 gives the bed height $H(t)$ as a function of time for different fluidizing velocities. The bed height is the average height of the top layer of spheres. The rise curves have been extrapolated to terminal rise for large times by a least-squares fit to $a + b\exp\{-ct\}$. For the case $V = 3\,\text{cm s}^{-1}$ we fit $H(t)$ to $a + b\exp\{-c(t-2)\}$ for $t > 2$ because the bed height first decreases. The terminal values

$$a = \lim_{t\to 0} H(t)$$

are given in table 1.

To test the effect of changing the size of the security zone in a relatively short time we studied the fluidization of 150 spheres rather than 1204 spheres. The size of the security zone was reduced to $h_v/2$. Figure 5 shows that the change in the height rise is modest: the smaller security zone allows for an increase in the bed height of about 2 or 3%.

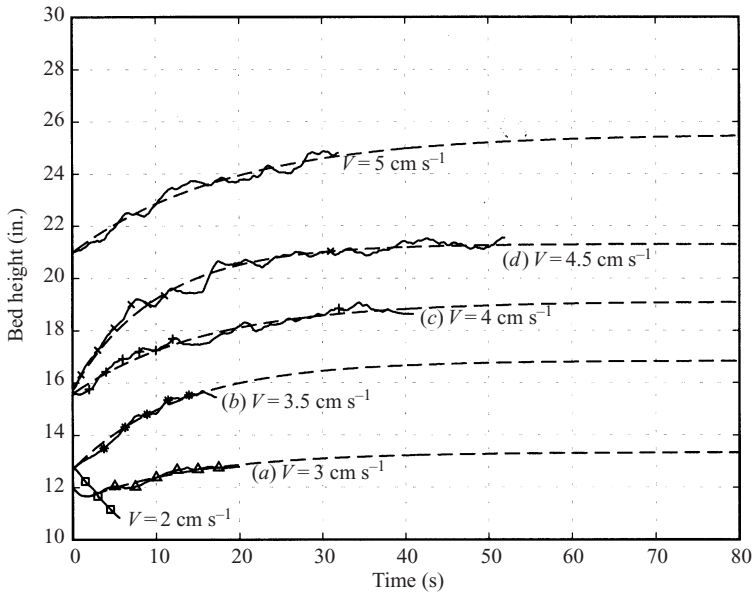

FIGURE 4. Bed height H vs. time for different values of the fluidizing velocity V. H is the average height of the top layer of 1204 spheres. The letters (a)–(d) refer to the snapshots shown in figures 9 and 10. The dashed lines are least-square fits to $H(t) = a + b\exp(-ct)$.

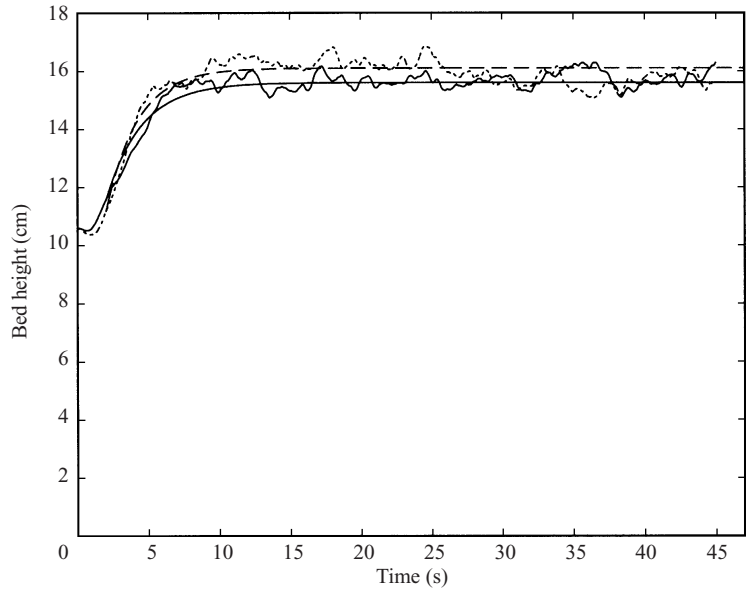

FIGURE 5. Bed height H vs. time for $V = 4\,\mathrm{cm\,s^{-1}}$. $H(t)$ is the average height of the top layer of 150 spheres. The straighter lines are least square fits to $H(t) = a + b\exp(-c(t-2))$. Dashed line, security zone $0.5\,h_v$; solid line, security zone h_v.

5. Qualitative comparison of experiment and simulation

The simulation was carried out in a fluidization column with coordinates shown in figure 6. In figures 7 and 8 snapshots of a simulation of 1204 spheres are shown in perspective to emphasize that the simulation is three-dimensional. The video animations

V (cm s^{-1})	a (in.)
3.0	13.33
3.5	16.84
4.0	19.10
4.5	21.29
5.0	25.52

TABLE 1. Terminal rise height a for different flow velocities.

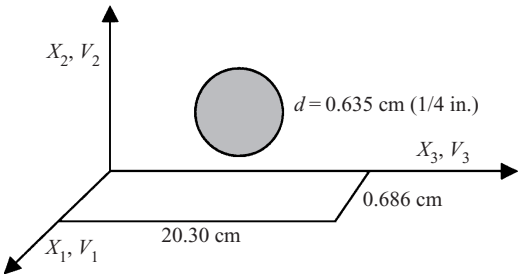

FIGURE 6. Coordinates and velocity components in the fluidization column. The fluidization velocity is $V \equiv V_2$.

of these simulations, which can be found at www.aem.umn.edu/Solid-Liquid_Flows, cannot be distinguished from real experiments. In figures 9 and 10 we compare snapshots of simulations in frontal view with snapshots from experiments under equivalent conditions. We also compare snapshots of simulations in frontal view for $V = 4\,\mathrm{cm\,s^{-1}}$ with snapshots from experiments under equivalent conditions for the case of $V = 4.037\,\mathrm{cm\,s^{-1}}$ in figures 11 and 12. We see that the simulation results do have features shown in the snapshots from experiments.

6. Numerical computation of averaged quantities

DLM produces huge amounts of data at each of millions of nodes. The problem is how to structure these data to extract useful information; we must decide beforehand what data to collect as values to store for post-processing. The fixed node property of DLM is well adapted to the collection of data in a form suitable for averaging methods used to construct models.

To define data structure we define a data string; this is a sequence of numbers produced at that node. We call the number of values in the data string the number of hits. In these simulations in which time steps are $\Delta t = 0.001$ s for start-up and 0.0005 s for the later times there may be 10 000 hits or more in a long simulation. Sometimes a particle is at the node; at the other times fluid is there. By processing data at hits we can create time averages without significant computational cost. Suppose a solid is at the node M times and the fluid is there M' times, $M + M' = 10^4$. Then $\phi = M/10^4$ and $\varepsilon = M'/10^4$, $\varepsilon + \phi = 1$ gives the volume fractions. If $V(\boldsymbol{x}, t)$ is the component of velocity parallel to gravity and $\boldsymbol{x}$ is at a node and $V_1(\boldsymbol{x}, t)$ is a data string of hits, then

$$V_s(\boldsymbol{x}, t) = \frac{1}{M} \sum_{i=1}^{M} V_i(\boldsymbol{x}, t) \tag{6.1}$$

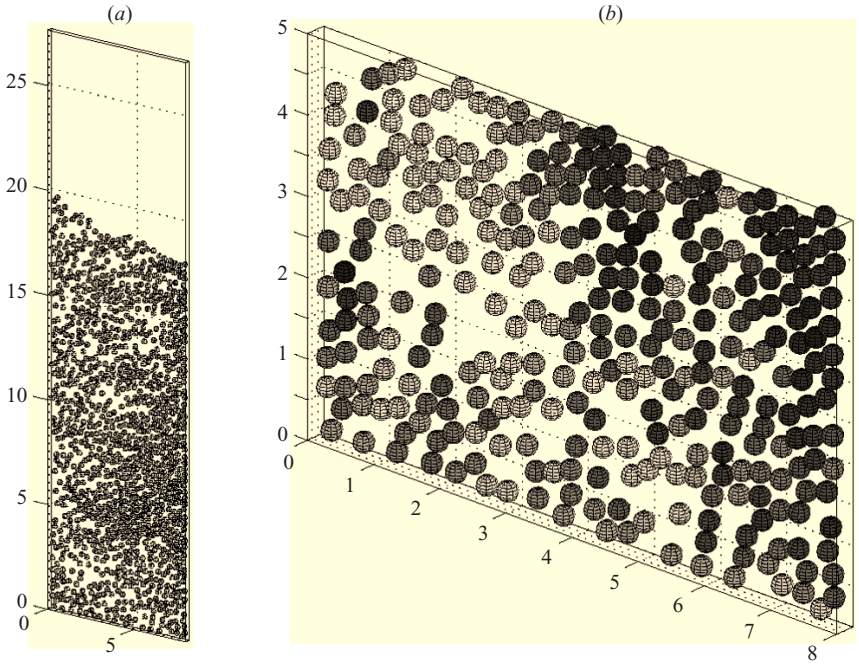

FIGURE 7. Snapshot of a simulation of 1204 spheres with $V = 4$ (a) and an enlargement (b), at $t = 32$.

where $\boldsymbol{x}$ is at a node; clearly

$$V_f(\boldsymbol{x}, t) = \frac{1}{M'} \sum^{M'} V_i(\boldsymbol{x}, t). \tag{6.2}$$

Then, at the same node, we should find

$$V(\phi) = V_s\phi + V_f\varepsilon. \tag{6.3}$$

After transients have disappeared in the fluidization we should find that $V_s = 0$.

In the same way, we can find a data string of values of the angular velocity as the difference of the velocity at a point in the solid and its mass centre and so on for other averages.

The time averages formed from data strings can be thought of as ensemble averages on non-transient flow and may be assumed to be local time averages on intervals with a sufficiently large number of hits which is small relative to the duration of transients. By repeating simulations we could initiate the procedure used to generate ensemble averages. There is a mathematical literature on the relation of time averages to ensemble averages which is rather theoretical and involves assumptions of a mathematical nature which are difficult to verify.

In our simulation of 1204 spheres we created such data strings at 38 nodes on a line across the width of the bed at a height of 10.179 in. in a plane in the centre of the depth, 0.135 in. from each wall. The width of the bed is 8 in. and the 38 nodes plus 2 wall points means that the nodes are separated by 1/10 in. The number of hits was $M = 7365$ for the case $V = 4.5\,\mathrm{cm\,s^{-1}}$ taken every 4 time steps. In figure 13 we present the solid fraction ϕ and the three components of the average solid V_s, liquid V_f and composite velocity $V(\phi) = V_s\phi + V_f(1-\phi)$ for the case $V = 4.5\,\mathrm{cm\,s^{-1}}$. The

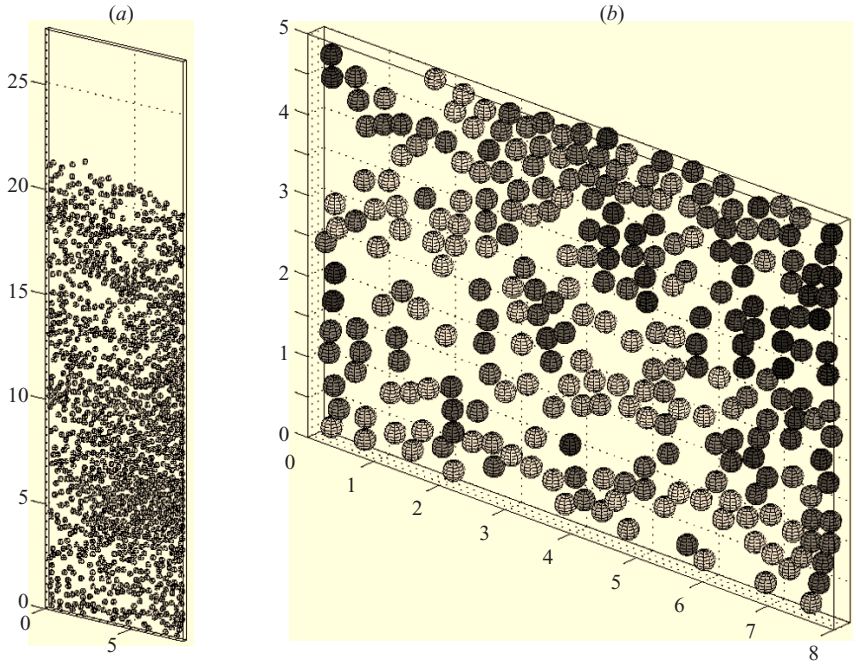

FIGURE 8. Snapshot of a simulation of 1204 spheres with $V = 4.5$ (*a*) and an enlargement (*b*), at $t = 31$.

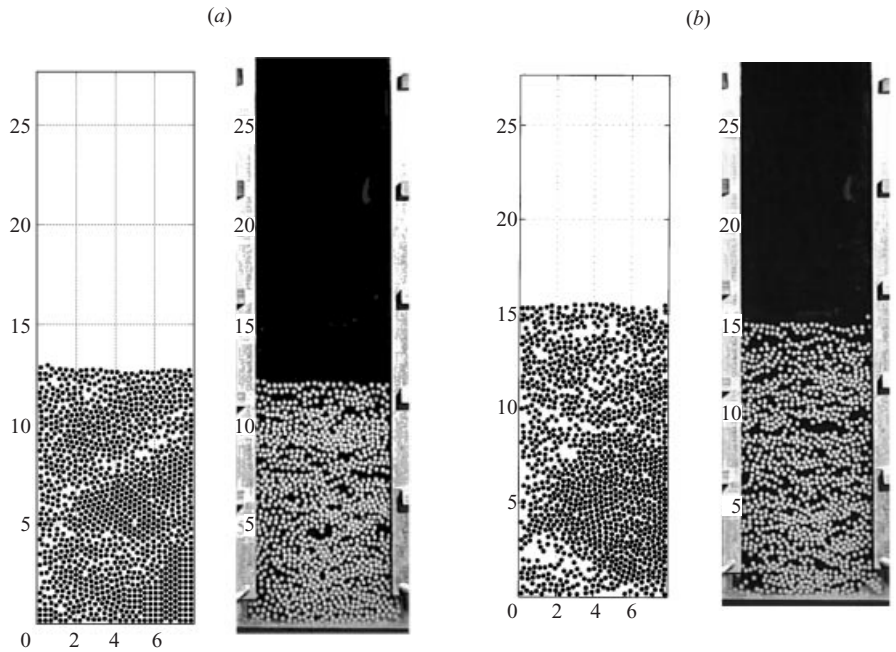

FIGURE 9. Comparison of frontal view snapshots of simulations (left) and experiments (right). (*a*) $V = 3$ cm s^{-1}, particle positions at $t = 20$ (corresponding to curve (*a*) of figure 4; maximum particle Reynolds number = 1142 (average 131)). (*b*) $V = 3.5$ cm s^{-1} at $t = 17.238$ (corresponding to curve (*b*) of figure 4; manimum particle Reynolds number = 1671 (average 236)).

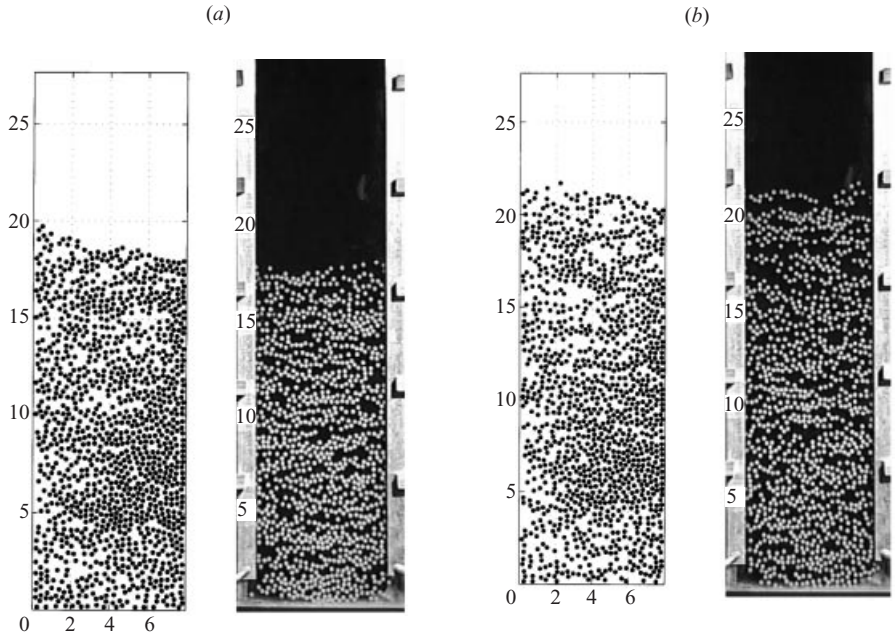

FIGURE 10. Comparison of frontal view snapshots of simulations (left) and experiments (right). (*a*) $V = 4$ cm s^{-1}, particle positions at $t = 32$ (corresponding to curve (*c*) of figure 4; maximum particle Reynolds number = 1965 (average 276)). (*b*) $V = 4.5$ cm s^{-1} at $t = 31$ (corresponding to curve (*d*) of figure 4; maximum particle Reynolds number = 1859 (average 292)).

velocity components V_1, V_2 and V_3 correspond to coordinates in the cross-section of the fluidization column shown in figures 13(*b*)–(*d*).

The data presented in figure 13 show that the dynamics of the bed are strongly two-dimensional, the velocity component V_2 is in the vertical direction; in the one-dimensional approximation the composite velocity

$$V_{2C}(\phi) = V_{2s}(\phi) + V_{2f}(1 - \phi)$$

would equal $V(\phi)$. Clearly, $V_2 = V_2(x_3)$ because of a large circulating eddy which is apparent on the video animations on http://www.aem.umn.edu/Solid-Liquid_Flows and in experiments. It is also apparent that the difference between averaged fluid velocity V_{2f} and the averaged solid velocity V_{2s} is positive; the solid lags the fluid by 3 to 5 cm s^{-1}. The transverse components of velocity V_1 and V_3 are basically zero, which is an assumption made in a one-dimensional theory. The fluctuation level of V_1 is very low because of the collision strategy interacting with nearby sidewalls, but the particles are not rigorously centred by these artificial collision forces.

It would be desirable to have many more points in our data strings. Greater computational efficiency and speed is a challenge for the future.

Figure 13 shows a strong two-dimensional variation of average equations across the slit column which is suppressed in one-dimensional studies.

7. Dynamic and wall friction pressure in a fluidized bed

The stress in an incompressible Newtonian fluid is given by

$$\boldsymbol{\sigma} = -P\mathbf{1} + 2\mu\boldsymbol{D}[\boldsymbol{u}] \tag{7.1}$$

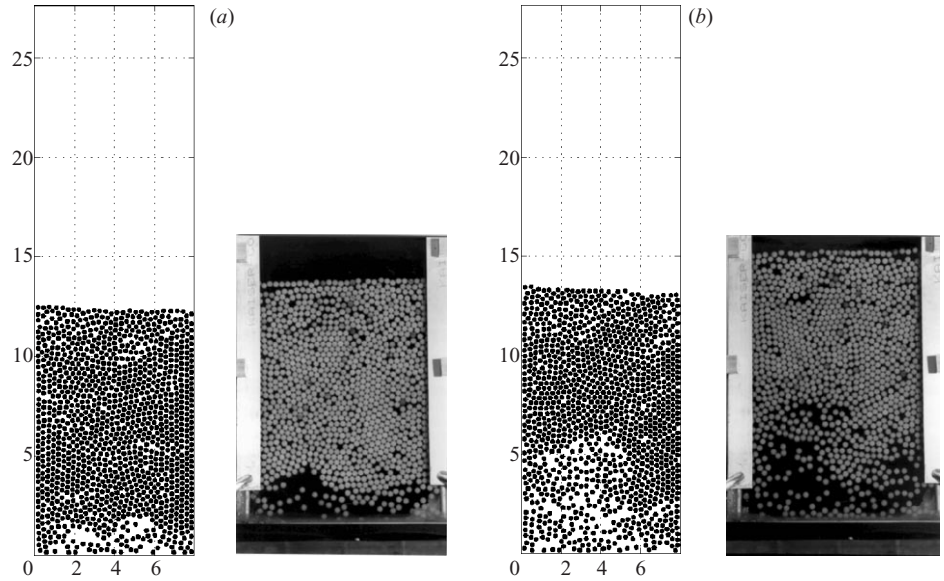

FIGURE 11. Comparison of snapshots of simulations for $V = 4$ cm s^{-1} at $t = 2$ (*a*) and 4 (*b*), and (right) snapshots from experiments under equivalent conditions for the case of $V = 4.037$ cm s^{-1}.

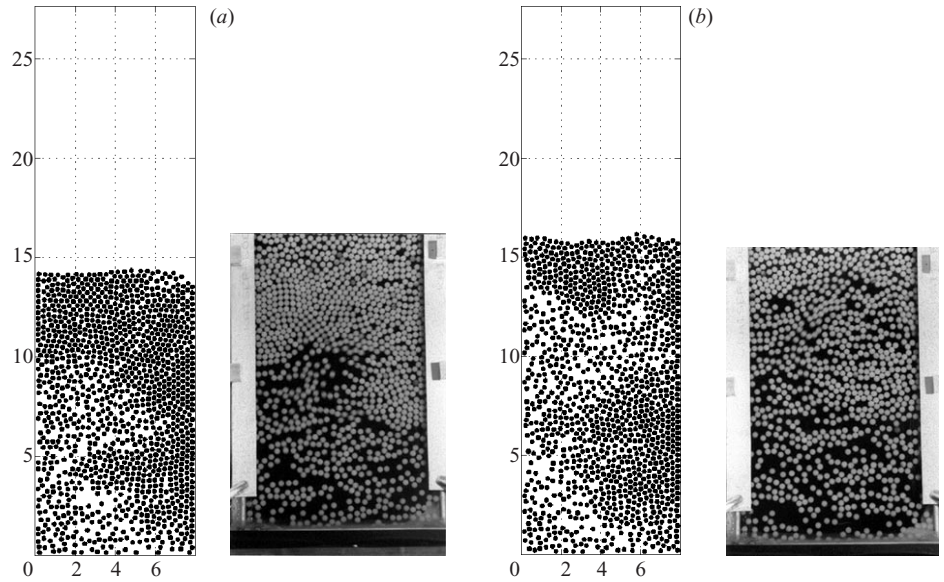

FIGURE 12. As figure 11 but at $t = 6$ (*a*) and 9 (*b*).

where $\boldsymbol{D}[\boldsymbol{u}]$ is the symmetric part of the velocity gradient $\nabla \boldsymbol{u}$ and P, the total pressure, is the mean normal stress. The equation of motion in the z-direction is

$$\rho \frac{\mathrm{d}w}{\mathrm{d}t} = -\frac{\mathrm{d}p}{\mathrm{d}z} + \mu \nabla^2 w, \tag{7.2}$$

where $w = \boldsymbol{e}_z \cdot \boldsymbol{u}$ and $p = P + \rho_f g z$ is the dynamic pressure that we compute in our DNS.

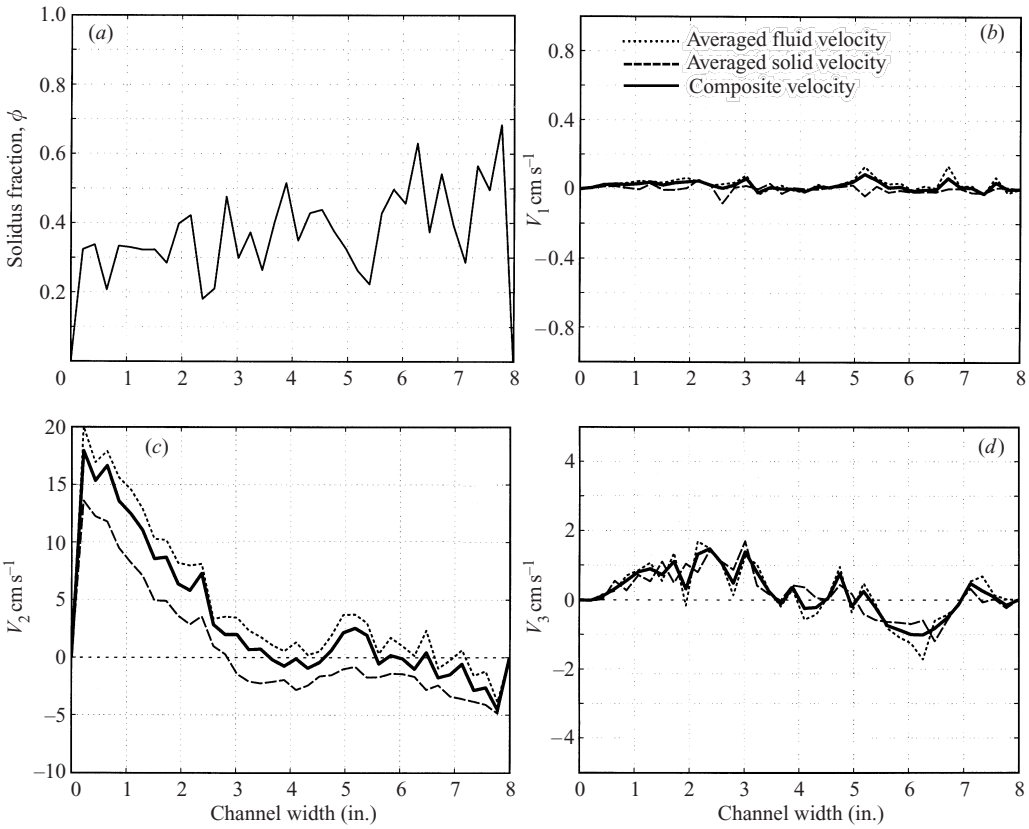

FIGURE 13. Volume fraction ϕ and averaged components of velocity V_1, V_2, V_3 in coordinate directions x_1, x_2, x_3 at 38 nodes spaced 1/10 in. apart across the 8 in. side of the fluidization column when $V = 4.5\,\mathrm{cm\,s^{-1}}$. (*a*) ϕ, (*b*) V_1, (*c*) V_2, (*d*) V_3. The difference between the averaged fluid and averaged solid velocity is the slip velocity. This is the first exact calculation of the slip velocity in a fluidized suspension.

We may compute an average dynamic pressure gradient $\mathrm{d}\bar{p}/\mathrm{d}z$ by averaging over cross-sections and time. This quantity then is given by DNS and is

$$\frac{\mathrm{d}\bar{p}}{\mathrm{d}z} = \frac{\mathrm{d}\bar{P}}{\mathrm{d}z} + \rho_f g. \tag{7.3}$$

We may decompose

$$\bar{p} = \bar{p}_w + \bar{p}_s, \tag{7.4}$$

where $\bar{p}_w$ is the wall friction pressure and $\bar{p}_s$ is the pressure required to fluidize the spheres. In fluidized bed practice it is assumed that when wall friction is negligible the pressure gradient

$$\frac{\mathrm{d}\bar{P}}{\mathrm{d}z} = -(\rho_P \phi + \rho_f \varepsilon)g = -\rho_c g \tag{7.5}$$

balances the composite weight of fluid plus solids. In this case

$$\frac{\mathrm{d}\bar{P}}{\mathrm{d}z} = \frac{\mathrm{d}\bar{p}}{\mathrm{d}z} - \rho_f g = \frac{\mathrm{d}\bar{p}_s}{\mathrm{d}z} - \rho_f g = -\rho_c g. \tag{7.6}$$

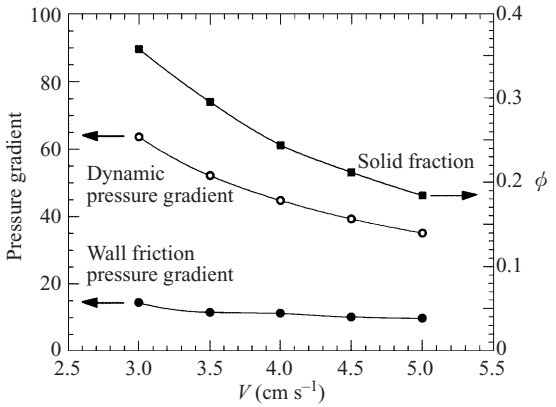

FIGURE 14. Solid fraction, dynamic pressure gradient and wall friction pressure gradient vs. fluidizing velocity.

Hence

$$\frac{\mathrm{d}\bar{p}_s}{\mathrm{d}z} = -(\rho_P - \rho_f)g\phi. \tag{7.7}$$

This expression was verified in experiments by Wilhelm & Kwauk (1948) and Lewis, Gilliand & Bauer (1949). Combining (7.4) and (7.7) we get

$$\frac{\mathrm{d}\bar{p}}{\mathrm{d}z} = \frac{\mathrm{d}\bar{p}_w}{\mathrm{d}z} - (\rho_P - \rho_f)g\phi. \tag{7.8}$$

When $\phi = 0$, the dynamic pressure is equal to the wall friction pressure.

Equation (7.8) is an equation for the wall friction pressure gradient with values of $\mathrm{d}\bar{p}/\mathrm{d}z$ and ϕ given by DNS. Table 2 gives the values of terms in this equation for different fluidizing velocities. The table shows that the wall friction pressure gradient is about 1/4 of the pressure gradient needed to fluidize the spheres. As V increases, ϕ decreases and the pressure gradient $(\rho_P - \rho_f)g\phi$ to fluidize spheres decreases. The small decrease in the wall friction pressure gradient with fluidizing is surprising; the wall friction should go up as the speed increases. We conjecture that the decreased friction is due to a decrease in the effective viscosity $\mu(\phi)$ of the mixture as ϕ is decreased; the viscosity of densely packed mixtures is greater.

The calculation given here points a new direction for the interrogation of DNS for new results in continuum engineering descriptions. Our conclusions are tentative because the results on the wall friction pressure gradient depend on the accuracy of our numerical simulation near walls. It is certainly true that the activation of a repelling force when the particle approaches the wall reduces accuracy. We are confident that the size of the security zone can be reduced to zero by techniques under development so the full hydrodynamics of lubricating flow can be captured up to mesh resolution.

8. Sedimentation and fluidization velocity of single spheres

We performed simulations and experiments on the sedimentation and fluidization velocity of single spheres. It is sometimes assumed that these two velocities are the same but in general this is true only in very special cases.

The flow of fluid up the slit bed is close to a developing Poiseuille flow in which the velocity of the fluid vanishes at the wall but not at the centre. In the sedimentation

V (cm s^{-1})	$-\frac{d\bar{p}}{dz}$ (dyn cm^{-2})	ϕ	$\rho_c g$	$(\rho_p - \rho_f)g\phi$	$-\frac{d\bar{p}_w}{dz} = -\frac{d\bar{p}}{dz} - (\rho_p - \rho_f)g\phi$
3.0	63.570	0.3582	1050.1	49.177	14.393
3.5	52.050	0.2956	1021.2	41.246	11.463
4.0	44.694	0.2439	1014.2	34.155	11.202
4.5	39.171	0.2119	1009.8	29.758	10.076
5.0	34.990	0.1842	1006.0	25.957	9.705

TABLE 2. Terms in the dynamic pressure gradient equation (7.8) $\rho_p = 1.14\,\mathrm{g\,cm^{-3}}$, $\rho_f = 1\,\mathrm{g\,cm^{-3}}$.

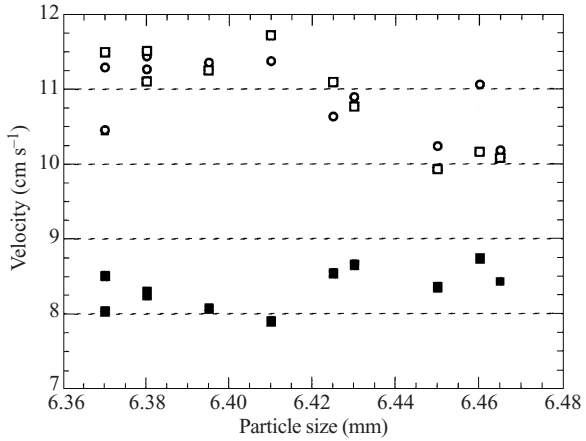

FIGURE 15. Sedimentation (◯) and fluidization velocities (□, ■) from experiments using different sized spheres. The particle lifts off the distributor when V is greater than ■ (the start fluidization) and is dragged out of the column only when V is greater than □ (escape fluidization).

case the fluid does not move unless disturbed by a falling particle. The flow of fluid in a fluidized bed need not be fully developed. The flow profile can change from station to station in the fluidized bed case, but not in the sedimentation case.

In the ideal case there is only one fluidization velocity and, if we ignore the flow variations just mentioned, this velocity is the sedimentation velocity; in both cases the drag balances the buoyant weight. For steady flow, fluidized and sedimenting particle velocities are equivalent under Galilean transformation. In fact we do not verify this ideal case in sedimentation or fluidization; a unique velocity does not emerge as can be seen from the experimental results given in figure 15, where we have plotted fluidization and sedimentation velocities for different spheres. Focusing first on sedimentation we note that even when we drop the same sphere in the quiet slit bed, the sedimentation velocity differs from trial to trial. Variations of as much as 7% are observed. How do we account for such variations?

As a practical matter our slit bed has a nominal gap size of 0.686 cm, but is certainly not uniform; perhaps it varies between 0.6778 and 0.7239 cm. Obviously this variation will lead to a variation in the sedimentation velocity.

A more fundamental reason for the variability in the sedimentation rate is that the motion at Reynolds numbers in the thousands is not steady and is probably chaotic in the sense of dynamical systems due to vortex shedding. The falling spheres do not centre rigorously but are in some kind of unsteady off-centre motion that is not

	Diameter			
	0.6300 cm	0.6350 cm	0.6398 cm	0.6500 cm
$h = 0.027$ in.	−8.085378	−8.130019	−8.155760	−7.790286
$h = 0.018$ in.	−8.722692	−8.738451	−8.689694	−8.724728

TABLE 3. Averaged vertical terminal velocities of spheres of different diameter and $\rho_p = 1.14\,\mathrm{g\,cm^{-3}}$ computed by DNS in the volume of figure 6.

understood well. How and why this kind of unsteadiness leads to different settling velocities is not understood.

Table 3 lists the values of the velocity of sedimenting spheres of different diameter falling in a 0.68 cm gap between the walls of the sedimentation column. The sedimentation velocity appears to increase rather markedly with mesh refinement; extrapolation to a fine mesh $h \to 0$ would seem to imply a fall of about $10\,\mathrm{cm\,s^{-1}}$ rather than the $8.7\,\mathrm{cm\,s^{-1}}$ value observed in the smaller mesh. We do not see a consistent variation with diameter. This may be due to some kind of unsteadiness to which we alluded in the previous paragraph. There is a discrepancy between the values in table 3 and those reported in the experiments of between 10% and 20% if $8.7\,\mathrm{cm\,s^{-1}}$ is taken as the representative simulation value. We think that it is probable that the faster fall velocity in the experiments may be due to channelling through places where the gap size is larger.

The fluidization results are of great interest. We do not obtain a unique fluidization velocity; for each sphere there is a rather large interval of velocities for which the sphere does not fall to the bottom or blow out of the bed. The interval may range, say from 6 to $11\,\mathrm{cm\,s^{-1}}$. For fluidization velocities less than, say $6\,\mathrm{cm\,s^{-1}}$, the sphere will not rise and for large velocities, say about $11\,\mathrm{cm\,s^{-1}}$, the sphere will blow out of the bed.

An important and practically useful result arising from this study of fluidization is that the height of the sphere above the bottom increases with the fluidizing velocity. This *positioning property* is such that the position of the particle in the bed may be controlled by setting the inlet flow rate. The positioning property also arises from our simulation and is clearly evident in the rise curves shown in figure 16. We have seen such positioning hydrodynamics in experiments on the fluidization of sensors in round pipes where the ability to position the sensor is of practical importance.

The positioning hydrodynamics is not understood. A promising explanation follows from the observation that the average distance between the particle and the wall is a function of the flow speed. Loosely, we could say that the Segré–Siberberg position of equilibrium between the centreline of close walls and the walls is a function of flow speed. The overall drag on the sphere, which in any case must balance the buoyant weight, is a function of flow speed and particle position. Evidently the flow speed produces a particle position such that the drag–weight balance is preserved at different heights in the bed.

In the simulation an exactly zero velocity of the sphere was not achieved. For $V \leqslant 6\,\mathrm{cm\,s^{-1}}$ the particle will not rise. The particle velocity in the interval of fluidization is very nearly zero and rather random as shown in table 4. The particle rises out of the bed when $V > 10.5\,\mathrm{cm\,s^{-1}}$.

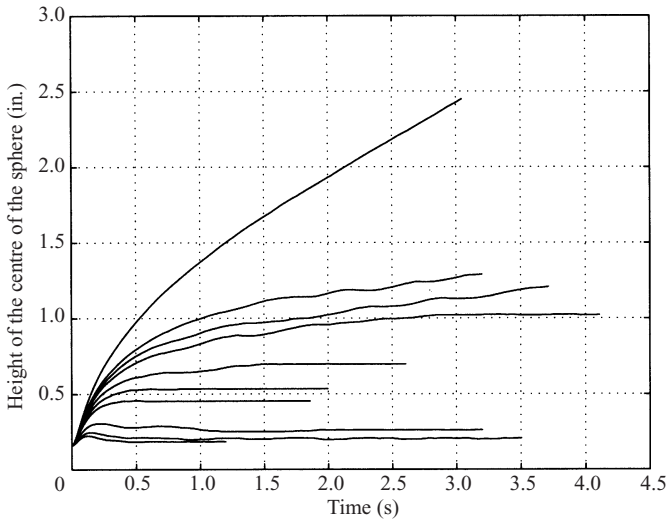

FIGURE 16. H vs. t for a single particle $d = 0.635\,\text{cm}$ from numerical simulation. For $V < V_m \approx 6\,\text{cm s}^{-1}$ the sphere remains at the distributor; for $V > V_m \approx 10.5\,\text{cm s}^{-1}$ the sphere is dragged out of the bed. Inflow speeds are 6, 6.5, 7.5, 9, 9.5, 10, 10.5, 10.75, 11, 12 cm s^{-1} from the bottom to the top respectively.

In-flow velocity (cm s^{-1})	Averaged vertical speed (after it has stabilized)
6.0	−0.00522
6.5	0.00827
7.5	0.00219
9.0	−0.00178
9.5	0.00631
10.0	0.0006997
10.5	0.00521
10.75	0.276
11.0	0.265
12.0	1.260

TABLE 4. The averaged vertical velocities of a sphere of diameter 0.63 cm fluidized in a two-dimensional-like bed of dimension $D \times W \times H = 0.27 \times 7.992 \times 8.1$ in. The sphere was initially located at the centre of the bottom of the bed.

9. Richardson–Zaki correlations from DNS

Here we introduce an application of DNS that we call the method of correlations. The method is inspired by the work of Richardson & Zaki (1954). They processed their data in log–log plots and found straight lines leading to power laws. The method of correlations follows the same procedure but using numerical data from DNS rather than experimental data. Data from our real and numerical experiments are shown in figure 17. The experiment and simulations do not quite match. The 1204 spheres used in the experiments are polydisperse (figure 3) with an average diameter of 0.6398 cm rather than the 0.635 cm diameter used in the simulation. Moreover the lowest data point for the simulation may be inaccurate because the artificial repulsive force which

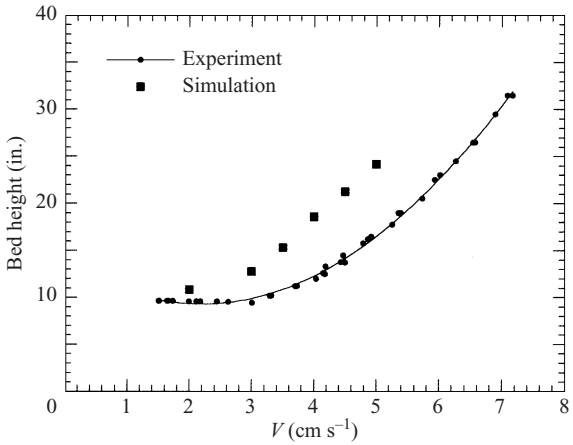

FIGURE 17. The bed height vs. fluidizing velocity for both experiment and simulation.

is activated to keep particles apart makes accurate calculations near close packing at incipient fluidization less accurate.

The Richardson–Zaki correlation relates the fluidization velocity $V(\phi)$ to the solid fraction $\phi = 1 - \varepsilon$, where ε is the fluid fraction, in a factored form in which $V(0)$, the blow-out velocity for a single sphere, is multiplied by a settling function. When $V > V(0)$ all the particles will be dragged out of the fluidized bed. For the monodispersed case studied in the rise height simulation

$$H_s = 4.564/(1 - \varepsilon). \tag{9.1}$$

The mean sphere size for the polydisperse case studied in the experiments is slightly larger and

$$H_e = 4.636/(1 - \varepsilon). \tag{9.2}$$

The Richardson–Zaki correlation is given by

$$V(\phi) = V(0)\varepsilon^{n(Re)} \tag{9.3}$$

where $V(0) = V$ when $\varepsilon = 1$, and

$$\left.\begin{aligned} n &= 4.65 + 19.5d/D \quad \text{when} \quad Re = V(0)d/v < 0.2, \\ n &= 4.36 + 17.6d/D \quad \text{when} \quad 0.2 < Re < 1, \\ n &= 4.45Re^{-1} \quad \text{when} \quad 1 < Re < 500, \\ n &= 2.39 \quad \text{when} \quad 500 < Re < 7000, \end{aligned}\right\} \tag{9.4}$$

and D is the tube radius. In our experiments and simulations Re is confined to the range for which $n = 2.39$.

The data shown in figure 17 is plotted in a log–log plot in figure 18 as V vs. ε. We draw a straight line with slope $n = 2.39$ through both sets of data. The fit is not perfect but is encouraging. From the straight lines we determine the blow-out velocities $V_s(0) = 8.131\,\mathrm{cm\,s^{-1}}$ and $V_e(0) = 10.8\,\mathrm{cm\,s^{-1}}$ and find the power laws

$$V_s(\phi) = 8.131\,\varepsilon^{2.39}\,\mathrm{cm\,s^{-1}}, \quad V_e(\phi) = 10.8\,\varepsilon^{2.39}\,\mathrm{cm\,s^{-1}}. \tag{9.5}$$

Different reasons could be considered for the discrepancy between numerical and experimental blow-out velocities. A referee of this paper suggested that tangential

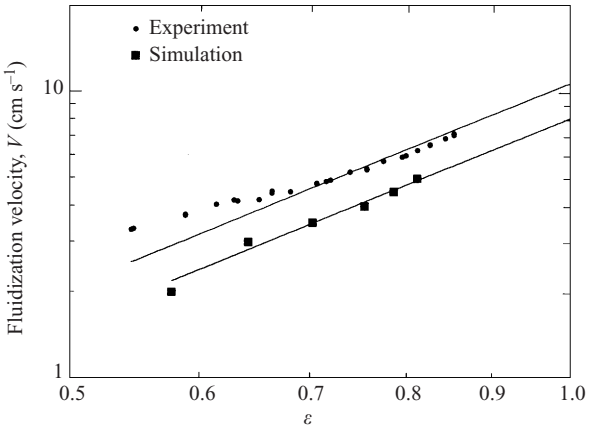

FIGURE 18. Data from figure 17 plotted in a log–log plot. The slopes of the straight lines are given by the Richardson–Zaki $n = 2.39$. The blow-out velocities $V_s(0)$ and $V_e(0)$ are defined as the intercepts at $\varepsilon = 1$.

lubrication forces are not accurately calculated by our numerical method. We think, however, that the discrepancy is due to the difference in the diameter, 0.635 cm, of the sphere in the simulation and average diameter 0.6398 cm of the 1204 spheres used in the experiments. This means that the walls will increase the drag more in the experiments than in the simulations. To estimate the effect we use the wall correction formula of Francis (1933), which was derived for Stokes settling of a sphere of diameter d in a tube of diameter D:

$$V(0) = \frac{\rho_s - \rho_f}{18\eta_f} d^2 \left(1 - \frac{d}{D}\right)^{2.25}. \tag{9.6}$$

If we take $D = 0.686$ cm, which is the distance between plane walls rather than a tube diameter, then the ratio of velocities corresponding to the nominal diameter d_1 and the average diameter d_2 is given by

$$\frac{V_s(0)}{V_e(0)} = \left(\frac{d_1}{d_2}\right)^{2.25} \left(\frac{D - d_1}{D - d_2}\right)^{2.25} = \left(\frac{6.35}{6.398}\right)^2 \left(\frac{51}{46.2}\right)^{2.25} = 1.233. \tag{9.7}$$

The value 1.233 is very close to the shift ratio

$$\frac{10.8}{8.131} = 1.248 \tag{9.8}$$

necessary to bring the straight lines in figure 18 together. After shifting by the value given in (9.8) we reverse the log–log plot to obtain the plot in figure 19.

10. Discussion

The fluidization of 1204 spheres at Reynolds numbers in the thousands was simulated using the method of distributed Lagrange multipliers. The results of the simulation are compared with a real experiment designed to match. This is the first direct numerical simulation of a real fluidized bed at the finite Reynolds numbers encountered in applications and the first attempt to match a real experiment to a fully resolved simulation. The numerical method used is currently far in advance of alternatives for fully resolved CFD approaches to solid–liquid flow. The experiments

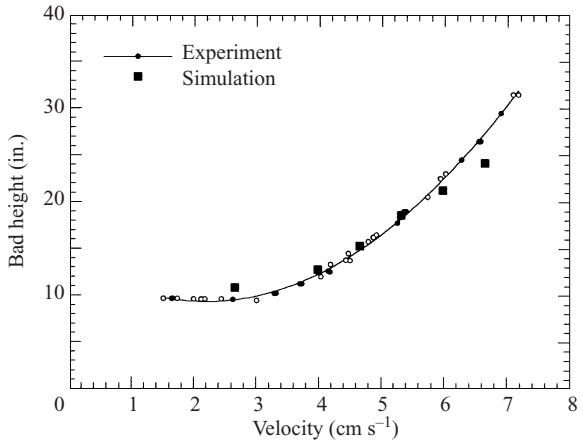

FIGURE 19. Bed height vs. fluidizing velocity after shifting by the ratio given in (9.8) of blow-out velocities obtained from the intercepts at $\varepsilon = 1$ in figure 18.

are carried out in a slit fluidization column in which the gap between close walls is slightly larger than the fluidized spheres. The match between theory and experiment is very good but not perfect: the spheres in the experiments are polydisperse with an average diameter of 0.6398 cm whereas all the spheres in the simulation are 0.635 cm in diameter. When these differences are factored into the comparison the simulations and experiments are in good quantitative agreement; the qualitative agreement is compelling. The emphasis of this paper is on the interrogation of DNS for results in multiphase fluid mechanics and introduces four new directions. First, we have shown how our numerical method can be used to generate averaged values of the solid fraction, the average of velocity components of both the solid and fluid and possibly other averaged values used in multiphase models; for example, we give the first numerical simulation of the slip velocity, which might be used in drift flux models. In a second application we obtain the contribution from wall friction that is usually neglected in one-dimensional models of the dynamic pressure in a fluidized flow. We find that in our slit bed the contribution of wall friction is about 1/4 of the total and that the contribution decreases modestly as the bed expands. Our comparative study of sedimentation and fluidization of single spheres revealed an unanticipated result that the balance between drag and buoyant weight can be achieved in an interval of velocities. We framed this result as a *positioning property*; the particle may be moved up and down the column by changing the fluidization velocity. The fluid mechanics here are not understood; we conjectured that the drag can be maintained as the velocity changes by a simultaneous change in the stand-off distance from the wall. The fourth and most important application was framed as the *method of correlations* inspired by the way that Richardson & Zaki (1954) processed their experimental results for power-law correlations. The idea is to plot results of experiments in log–log plots. Remarkably, straight lines emerge. Apparently the flow of dispersions is governed at the foundation by similarity rules which are not at all evident. We implemented this method using numerical rather than real experiments and we think that our results establish this concept: the results in the experiments and simulations do follow the Richardson–Zaki correlation in a compelling if not perfect match. We prefer to frame our result as a demonstration

that we can generate power laws by processing DNS data, rather than confirming correlations already obtained. We intend to promote this approach strongly in the future.

We acknowledge the support by NSF (grants ECS-9527123 and CTS-9873236) and the Minnesota Supercomputing Institute. The work of Glowinski and Pan was also supported by the Texas Board of Higher Education (ARP grant 003652-0383-1999) and NSF DMS-9973318. Joseph's work was also supported by NSF GOALI grant and by DOE, Programming of Engineering Research, Department of Basic Energy Sciences. We also thank N. A. Patankar for his helpful discussion.

REFERENCES

Aidun, C. K. & Lu, Y. 1995 Lattice Boltzmann simulation of solid particles suspended in fluid. *J. Statist. Phys.* **81**, 49–61.

Aidun, C. K., Lu, Y. & Ding, E. 1998 Direct analysis of particulate suspensions with inertia using the discrete Boltzmann equation. *J. Fluid Mech.* **373**, 287–311.

Barenblatt, G. J. 1996 *Scaling, Self-similarity, and Intermediate Asymptotics.* Cambridge University Press.

Brady, J. F. 1993 Stokesian dynamics simulation of particulate flows in particulate two-phase flow. In *Particulate two-phase flow* (ed. M. Roco), pp. 971–998. Butterworth–Heinemann.

Bristeau, M. O., Glowinski, R. & Periaux, J. 1987 Numerical methods for the Navier–Stokes equations. Applications to the simulation of compressible and incompressible viscous flow. *Computer Phys. Rep.* **6**, 73–187.

Chorin, A. J. 1967 A numerical method for solving incompressible viscous flow problems. *J. Comput. Phys.* **2**, 12–26.

Chorin, A. J. 1968 On the convergence and approximation of discrete approximation to the Navier–Stokes equations. *Math. Comput.* **23**, 341–353.

Chorin, A. J. 1973 Numerical study of slightly viscous flow. *J. Fluid Mech.* **57**, 785–796.

Crowe, C. T., Chung, J. N. & Troutt, T. R. 1996 Numerical models for two-phase turbulent flows. *Annu. Rev. Fluid Mech.* **28**, 11–43.

Francis, A. W. 1933 Wall effect in falling ball method for viscosity. *Physics* **4**, 403–406.

Glowinski, R., Hesla, T., Joseph, D. D., Pan, T.-W. & Periaux, J. 1997 Distributed Lagrange multiplier methods for particulate flows. In *Computational Science for the 21st Century* (ed. M. O. Bristeau, G. Etgen, W. Fitzgibbon, J. L. Lions, J. Periaux & M. F. Wheeler), pp. 270–279. Wiley.

Glowinski, R., Pan, T.-W., Hesla, T. & Joseph, D. D. 1999 A distributed Lagrange multiplier/fictitious domain method for flows around moving rigid bodies: Application to particulate flows. *Intl J. Multiphase Flow* **25**, 755–794.

Glowinski, R., Pan, T.-W., Hesla, T., Joseph, D. D. & Periaux, J. 1998 A fictitious domain method with distributed Lagrange multipliers for the numerical simulation of particulate flow. In *Domain Decompositon Methods 10* (ed. J. Mandel, C. Farhat & X. C. Cai), pp. 121–137. American Mathematical Society, Providence, RI.

Glowinski, R., Pan, T.-W., Hesla, T., Joseph, D. D. & Periaux, J. 2001 A fictitious domain approach to the direct numerical simulation of incompressible viscous flow past moving rigid bodies: application to particulate flow. *J. Comput. Phys.* **169**, 363–426.

Hofler, K., Muller, M., Schwarzer, S. & Wachmann, B. 1999 Interacting particle-liquid systems. In *High Performance Computing in Science and Engineering '98* (ed. E. Krause & W. Jager), pp. 54–64. Springer.

Johnson, A. & Tezduyar, T. E. 1999 Advanced mesh generation and update methods for 3D flow simulations. *Computat. Mech.* **23**, 130–143.

Ladd, A. J. C. 1994*a* Numerical simulations of particulate suspensions via a discretized Boltzmann equation. Part 1. Theoretical foundation. *J. Fluid Mech.* **271**, 285–309.

Ladd, A. J. C. 1994*b* Numerical simulations of particulate suspensions via a discretized Boltzmann equation. Part 2. Numerical results. *J. Fluid Mech.* **271**, 311–339.

Ladd, A. J. C. 1996 Hydrodynamic screening in sedimenting suspensions of non-Brownian spheres. *Phys. Rev. Lett*. **76**, 1392–1395.

Ladd, A. J. C. 1997 Sedimentation of homogeneous suspensions of non-Brownian spheres. *Phys. Fluids* **9**, 491–499.

Lewis, W. K., Gilliand, E. R. & Bauer, W. C. 1949 Characteristics of fluidised particles. *Indust. Engng Chem.* **41**, 1104.

Marchuk, G. I. 1990 Splitting and alternating direction methods. In *Handbook of Numerical Analysis, Vol. 1* (ed. P. G. Ciarlet & J. L. Lions), pp. 197–462. North-Holland.

Maxey, M. R. & Patel, B. K. 1997 Force-coupled simulations of particle suspensions at zero and finite Reynolds numbers. *ASME FEDSM* 97-3188.

Maxey, M. R., Patel, B. K., Chang, E. J. & Wang, L. P. 1997 Simulations of dispersed turbulent multiphase flow. *Fluid Dyn. Res.* **20**, 143–156.

McLaughlin, J. B. 1994 Inertial computation of particle turbulent interaction. *Intl J. Multiphase Flow* **20**, 211–232.

Ory, E., Oguz, H. N. & Prosperetti, A. 2000 Physalis: a new $O(N)$ method for the numerical simulation of particle flows. *Proc. ASME FEDSM'00, ASME 2000 Fluids Engineering Divisions Summer Meeting, June 11–15, Boston, MA*.

Pan, T.-W., Sarin, V., Glowinski, R., Sameh, A. & Periaux, J. 1999 A fictitious domain method with distributed Lagrange multipliers for the numerical simulation of particular flow and its parallel implementation. In *Parallel Computational Fluid Dynamics, Development and Applications of Parallel Technology* (ed. C. A. Lin, A. Ecer, N. Satofuka, P. Fox & J. Periaux), pp. 467–474. North-Holland.

Patankar, N. A., Huang, P. Y., Ko, T. & Joseph, D. D. 2001*a* Lift-off of a single particle in Newtonian and viscoelastic fluids by direct numerical simulation. *Fluid Mech.* **438**, 67–100.

Patankar, N., Ko, T., Choi, H. G. & Joseph, D. D. 2001*b* A correlation for the lift-off of many particles in plane Poiseuille flows of Newtonian fluids. *J. Fluid Mech.* **445**, 55–76.

Peskin, C. S. 1977 Numerical analysis of blood flow in the heart. *J. Comput. Phys.* **25**, 220–252.

Peskin, C. S. 1981 *Lectures on Mathematical Aspects of Physiology*. Lectures in Applied Mathematics, vol. 19, pp. 69–107. Springer.

Peskin, C. S. & McQueen, D. M. 1980 Modeling prosthetic heart valves for numerical analysis of blood flow in the heart. *J. Comput. Phys.* **37**, 113–132.

Qi, D. 1997 Non-spheric colloidal suspensions in three-dimensional space. *Intl J. Mod. Phys.* C **8**, 985–997.

Qi, D. 1999 Lattice Boltzmann simulations of particles in non-zero Reynolds number flows. *J. Fluid Mech.* **385**, 41–62.

Richardson, J. F. & Zaki, W. N. 1954 Sedimentation and fluidization: Part I. *Trans. Inst. Chem. Engrs* **32**, 35–53.

Sarin, V. & Sameh, A. 1998 An efficient iterative method for the generalized Stokes problem, *SIAM J. Sci. Comput*. **19**, 206–226.

Singh, P., Hesla, T. I. & Joseph, D. D. 2001 A modified distributed Lagrange multiplier/fictitious domain method for particulate flows with collisions. *Intl J. Multiphase Flow* (submitted).

Wachmann, B., Kalthoff, W., Schwarzer, S. & Hermann, H. 1998 Collective drag and sedimentation: comparison of simulation and experiment in two and three dimensions. *Granular Matter* **1**(2), 75–82.

Wachmann, B. & Schwarzer, S. 1998 Three-dimensional massively parallel computing of suspensions. *Intl J. Mod. Phys.* C **9**(5), 759–775

Wilhelm, R. H. & Kwauk, M. 1948 Fluidization of solid particles. *Chem. Engng Prog*. **44**, 201.